

Electroviscous drag on squeezing motion in sphere-plane geometry

Marcela Rodríguez Matus^{1*}, Zaicheng Zhang^{1*}, Zouhir

Benrahla^{1*}, Arghya Majee², Abdelhamid Maali¹, Alois Würger¹

¹Université de Bordeaux & CNRS, Laboratoire Ondes et Matière d'Aquitaine, 33405 Talence, France

²Max Planck Institute for Intelligent Systems, Stuttgart, Germany & IV. Institute for Theoretical Physics, University of Stuttgart, Germany

Theoretically and experimentally, we study electroviscous phenomena resulting from charge-flow coupling in a nanoscale capillary. Our theoretical approach relies on Poisson-Boltzmann mean-field theory and on coupled linear relations for charge and hydrodynamic flows, including electro-osmosis and charge advection. With respect to the unperturbed Poiseuille flow, we define an electroviscous coupling parameter ξ , which turns out to be maximum where the film height h_0 is comparable to the Debye screening length λ . We also present dynamic Atomic Force Microscope (AFM) data for the visco-elastic response of a confined water film in sphere-plane geometry; our theory provides a quantitative description for the electroviscous drag coefficient and the electrostatic repulsion as a function of the film height, with the surface charge density as the only free parameter. Charge regulation sets in at even smaller distances.

I. INTRODUCTION

Solid surfaces in contact with water are mostly charged, resulting in intricate interactions of the diffuse layer of counterions with liquid flow along the solid boundary [1–3]. Charge-flow coupling is at the origin of various electro-kinetic and electric-viscous effects [4]. Besides classical applications of capillary electrophoresis ranging from microfluidics to medical analysis, recently AC charge-induced electro-osmosis has been used for the assembly of active materials from micron-size colloidal building blocks [5], surface osmotic effects have been discussed in view of energy applications and desalination of sea water [6].

The underlying physical mechanisms operate on the scale of the Debye screening length [7], which is of the order of a few tens of nanometers. Following the derivation of the electroosmotic coefficient by Helmholtz [8] and Smoluchowski [9], electrokinetic effects have been extensively studied in the limit of thin double layers, where the screening length is much smaller than the depth of the liquid phase. Thus Bikerman [10] and Dukhin [3] derived the surface contribution to the electric conductivity of an salt solution, and Hückel [11] and Henry [12] showed the colloidal electrophoretic mobility to depend on the ratio of particle size and screening length. Gross and Osterle studied charged membranes separating two electrolyte solutions at different pressure and electro-chemical potentials, and numerically calculated the transport coefficients of nanopores comparable to the screening length [13].

Prieve and collaborators studied charge effects on the motion of a colloidal sphere moving close to a solid surface [14–18]. For a particle sliding parallel to the surface at velocity V , they observed a normal lift force proportional to V^2 . This dependence suggests as underlying mechanism the Maxwell stress ϵE^2 , with the permittivity ϵ and the parallel electric field arising from the streaming potential, $E \propto V$ [15]. Yet the measured lift force [17]

by far exceeds the calculated value [18]; this discrepancy has not been elucidated so far.

Quite a different situation occurs for the squeezing motion of a colloidal sphere vibrating in normal direction with a sinusoidal displacement $Z(t)$, as shown schematically in Fig. 1. The velocity $V = dZ/dt$ is by orders of magnitude smaller than that of sliding motion, resulting in a negligibly weak electrokinetic lift. For uncharged surfaces, the only force at work is the hydrodynamic drag $-\gamma_0 V$ with coefficient γ_0 . The presence of electric double layers gives rise to several electrokinetic forces,

$$K - kZ - \gamma V, \quad (1)$$

where the electrostatic repulsion K is well known from static Atomic Force Microscope (AFM) experiments [19]. For a mechanically driven system as in Fig. 1, the dynamic response consists of a restoring force $-kZ$ with an effective spring constant k and an enhanced drag coefficient γ , due to the coupling of the charged diffuse

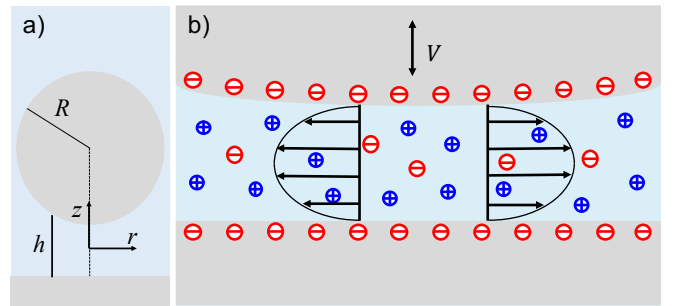


FIG. 1. Schematic view of charge-flow coupling in sphere-plane geometry. a) A colloidal sphere of radius R is placed above a solid surface. The film height h varies with the radial coordinate r and takes its minimum value h_0 at $r = 0$; this distance satisfies $h_0 \ll R$. b) The sphere vertically vibrates with velocity $V(t)$. This squeezing motion induces a radial Poiseuille flow in the confined water film containing mobile ions of either sign.

layers to the radial flow profile [20, 21]. Bike and Prieve calculated the charge contribution $\gamma - \gamma_0$ for the case where the sphere-plane distance h_0 is much larger than the Debye screening length λ [15]. Subsequent numerical studies discussed the enhancement factor for both narrow and wide channels, and found a maximum to occur at $\lambda/h_0 \approx 1$ [22, 23]. The first unambiguous experimental observation of the electroviscous effect was reported very recently by Liu et al, who performed dynamic AFM experiments in weak electrolyte solutions [21].

The present work intends to clarify whether charge-flow coupling accounts quantitatively for the electroviscous drag on the squeezing motion illustrated in Fig. 1. Section II provides a brief reminder of Poisson-Boltzmann theory, and the static repulsive force K and the spring constant k . In Section III we develop the formal apparatus for charge-flow coupling, relying on Onsager's phenomenological relations for generalized fluxes and forces, without resorting to the linearization approximation in the electroviscous coupling parameter. We derive the electroviscous drag coefficient γ in terms of the Onsager transport coefficients L_{ij} . In Section IV we compare analytical approximations for the limiting cases of narrow and wide channels with the numerical computation. Section V is devoted to a discussion of the effect of charge regulation on both electrostatic and electroviscous properties. In Sect. VI we present dynamic-AFM measurements and compare with our theoretical findings.

II. ELECTROSTATICS

Here we briefly discussed the electrostatic properties in the absence of external driving. Solid materials in contact with water in general carry surface charges. Due to electrostatic screening, the released counterions are confined in a diffuse layer of charge density ρ , which is related to the electrostatic potential ψ through Gauss's law

$$\nabla^2 \psi = -\frac{\rho}{\varepsilon}. \quad (2)$$

In the framework of Poisson-Boltzmann mean-field theory the concentrations of monovalent ions read $n_{\pm} = n_0 e^{\mp e\psi/k_B T}$, where the bulk value n_0 corresponds to dissolved salt, to carbonic acid absorbed from air or to the dissociation of water. The resulting expression for the charge density

$$\rho = e(n_+ - n_-) = 2en_0 \sinh \frac{e\psi}{k_B T} \quad (3)$$

then closes Gauss's law.

A. 1D Poisson-Boltzmann theory

This work deals with thin films as in Fig. 1, where the minimum height is much smaller than the radius of

the vibrating sphere, $h_0 \ll R$. Then electrostatic and hydrodynamic properties are relevant in the lubrication area only, which corresponds to the range where the radial coordinate r takes values much smaller than R and where the height $h(r)$ of the aqueous film is a slowly varying function of r . For notational convenience we define the origin of the vertical coordinate z such that the solid boundaries are at $z = \pm h/2$.

Throughout this paper we assume a homogeneous surface charge and use the 1D Poisson-Boltzmann equation where ψ and ρ depend on the vertical coordinate z only,

$$\frac{e}{k_B T} \frac{d^2 \psi}{dz^2} = \lambda^{-2} \sinh \frac{e\psi}{k_B T}, \quad (4)$$

Here we introduce two characteristic length scales, the Debye screening length

$$\lambda = \frac{1}{\sqrt{8\pi n_0 \ell_B}} \quad (5)$$

which gives the thickness of the diffuse layer in an electrolyte solution [24], and the Bjerrum length

$$\ell_B = \frac{e^2}{4\pi\varepsilon k_B T} \quad (6)$$

which gives the distance where the electrostatic interaction of two elementary charges is equal to the thermal energy. Typical values in water are $\lambda = 1...300$ nm and $\ell_B = 0.7$ nm

For fixed surface charge density $e\sigma$, the potential satisfies the boundary condition

$$\frac{e\sigma}{\varepsilon} = \mp \left. \frac{d\psi}{dz} \right|_{z=\pm h/2}. \quad (7)$$

For fixed surface potential one has $\psi(\pm h/2) = \zeta$. Note that the potential $\psi(z)$ and its surface value ζ depend on the film height h and thus on r .

B. Disjoining pressure and repulsive force

For the sake of notational simplicity we assume a symmetric system with the same charge density σ on the two opposite surfaces. Then the disjoining pressure is given by the excess osmotic pressure of the mobile ions at $z = 0$, which reads $\Pi = (n_m - 2n_0)k_B T$. With the excess number density $n_m = 2n_0 \cosh(\psi(0)/k_B T)$, one readily finds

$$\Pi = 2n_0 k_B T \left(\cosh \frac{e\psi(0)}{k_B T} - 1 \right). \quad (8)$$

The dependence of the osmotic pressure on the film height h arises from the potential $\psi(z=0)$ [24]. At distances h larger than the screening length λ , this potential vanishes, and so does the disjoining pressure.

The repulsive force K between the two surfaces, is obtained as the surface integral the osmotic pressure. The film height being much smaller than the curvature radius, we use the Derjaguin approximation [25]. For distances much smaller than the radius of the oscillating sphere, the height of the water film $h = h_0 + R - \sqrt{R^2 - r^2}$ is well approximated by

$$h(r) = h_0 + \frac{r^2}{2R}, \quad (r \ll R). \quad (9)$$

Writing the surface element as $dS = 2\pi r dr = 2\pi R dh$, one readily obtains

$$K(h_0) = \int dS \Pi = 2\pi R \int_{h_0}^{\infty} dh \Pi(h). \quad (10)$$

The disjoining pressure gives rise to a static restoring force $-kZ$, with spring constant

$$k(h_0) = -\frac{dK}{dh_0} = 2\pi R \Pi(h_0). \quad (11)$$

The discussion and numerical evaluation of the force K and the rigidity k are postponed to Sect. V below.

III. CHARGE-FLOW COUPLING: FORMAL APPARATUS

Here we derive the formal expression for the electroviscous drag coefficient γ defined in (1). Resorting to lubrication approximation, we give the coupled hydrodynamic and charge flows in radial direction, which are imposed by the mechanical driving, as illustrated in Fig. 1. Then we derive expressions for the hydrodynamic pressure and the resulting drag force.

We consider charged surfaces in sphere-plane geometry, in contact with an electrolyte solution, as shown schematically in Fig. 1. The vertical distance varies with time according to $h_0 + Z(t)$, with a small sinusoidal amplitude $|Z| \ll h_0$ and frequency ω , resulting in the velocity $V = dZ/dt$. Experimentally, this is realized by a vibrating sphere of radius R mounted on the cantilever of an AFM.

A. Lubrication approximation

The vertical oscillation modulates the hydrodynamic pressure P in the film and imposes a flow J_V . For an incompressible fluid, there is a simple geometrical relation between the vertical velocity V of the cantilever and the volume flow carried by the radial fluid velocity v ,

$$\pi r^2 V = 2\pi r J_V = 2\pi r \int_{-h/2}^{h/2} dz v(z, r). \quad (12)$$

Note that the height $h(r)$ varies with the radial position r according to (9).

The fluid mechanical problem simplifies significantly when resorting to the lubrication approximation [26]. In the range of validity of Eq. (9), the vertical component of the velocity field is negligible, and the radial component v obeys a simplified Stokes equation,

$$\eta \partial_z^2 v = \partial_r P - \rho E, \quad (13)$$

with the viscosity η and where only the vertical component of the Laplace operator $\nabla^2 v$ has been retained. The right-hand side comprises the radial pressure gradient $\partial_r P$ and the force exerted by a radial electric field E and the charge density ρ of the diffuse layer.

B. Non-equilibrium fluxes and forces

Using the Derjaguin approximation, the electrostatic properties can be calculated from the 1D Poisson-Boltzmann equation (4) with slowly varying gap height $h(r)$. Yet this equilibrium state is perturbed by charge-flow coupling. Indeed, advection of counterions by the radial velocity v , results in a radial charge distribution and an electric field E . Through the electro-osmotic force ρE in (13), the field backreacts on the flow properties.

For an axisymmetric geometry, both E and the pressure P depend on the radial coordinate r only, and the velocity field $v = v_P + v_E$ and charge current $j = j_P + j_E$ point in radial direction. Integrating over the vertical variable z we obtain the fluxes of volume and charge,

$$J_V = \int_{-h/2}^{h/2} dz (v_P + v_E) \equiv -L_{vv} \nabla P + L_{vc} E, \quad (14)$$

$$J_C = \int_{-h/2}^{h/2} dz (j_P + j_E) \equiv -L_{cv} \nabla P + L_{cc} E, \quad (15)$$

where the second identity defines the linear transport coefficients L_{ij} with respect to the generalized forces $-\nabla P = -dP/dr$ and eE .

The first term in eq. (14) arises from the pressure driven flow profile $v_P(z)$. Assuming no-slip boundary conditions $v_P(\pm h/2) = 0$, the Stokes equation (13) with $E = 0$ is readily integrated,

$$v_P = -\frac{h^2 - 4z^2}{8\eta} \nabla P, \quad (16)$$

resulting in

$$L_{vv} = \frac{h^3}{12\eta}. \quad (17)$$

The second term in (14) accounts for the electro-osmotic velocity profile [27]

$$\begin{aligned} v_E(z) &= -\frac{1}{\eta} \int_z^{h/2} dz' \int_0^{z'} dz'' \rho(z'') E \\ &= \frac{\varepsilon}{\eta} (\psi(z) - \zeta) E, \end{aligned} \quad (18)$$

where the second identity follows from twice integrating Gauss' law $\varepsilon\partial_z^2\psi = -\rho$. This leads to the electro-osmotic transport coefficient

$$L_{vc} = \frac{1}{E} \int_{-h/2}^{h/2} dz v_E(z). \quad (19)$$

The electric current (15) consists of advection of counterions in the Poiseuille flow profile v_P ,

$$L_{cv} = \frac{1}{\eta} \int_{-h/2}^{h/2} dz \rho(z) \frac{h^2 - 4z^2}{8}, \quad (20)$$

and Ohm's law with the conductivity L_{cc} . This latter coefficient reads as

$$L_{cc} = \int_{-h/2}^{h/2} dz \left(\rho \frac{\varepsilon}{\eta} (\psi - \zeta) + e^2 (\mu_+ n_+ + \mu_- n_-) \right) \quad (21)$$

where the first term accounts for advection by the electro-osmotic velocity field v_E , and the second one for electrophoresis of salt ions, with mobilities μ_{\pm} .

Electrokinetic phenomena in a channel between two electrolyte reservoirs at different electrochemical potential, are characterized by a constant streaming current $J_C \neq 0$ [6, 13, 14]. Contrary to this open geometry, the periodically driven squeezing motion of Fig. 1 does not allow for a steady current but gives rise to the electric field E . Strictly speaking, there is a small current which develops the space charges related to the electric field, $\delta\rho = \varepsilon \text{div} \cdot E$, and which vanishes when averaged over one cycle. Because of the strong electric interactions, the space charges develop almost instantaneously such that the electric field is in phase with the pressure gradient, and that advection and conduction currents cancel each other in (15),

$$J_C = 0. \quad (22)$$

This relation holds true as long as the charge relaxation time τ is much shorter than the period of the external driven, $\omega\tau \ll 1$.

C. Drag force

With the above condition of zero charge current, eq. (15) implies a relation between the radial electric field and the pressure gradient,

$$E = \frac{L_{cv}}{L_{cc}} \nabla P. \quad (23)$$

Inserting this in the volume current (14) and solving for the pressure gradient, we find

$$\nabla P = -\frac{6\eta r V}{h^3} \frac{1}{1 - \xi}, \quad (24)$$

where the coupling of the double layer to the flow is accounted for by the ratio of off-diagonal and diagonal transport coefficients L_{ij} ,

$$\xi = \frac{L_{vc} L_{cv}}{L_{vv} L_{cc}}. \quad (25)$$

From (24) it is clear that the dimensionless parameter ξ describes the effect of charge-flow coupling on the hydrodynamic pressure. For $\xi = 0$ one recovers the well-known expression for the pressure gradient in capillary. The stability of the dynamic equations (14) and (15) requires a positive determinant of the matrix of the transport coefficients L_{ij} , that is $\det \mathbf{L} > 0$ or $\xi < 1$.

When integrating the excess hydrodynamic pressure in the capillary, it turns out convenient to use the variable h instead of r . In lubrication approximation (9) one has $dh = dr r/R$ and

$$P(h) = 6\eta R V \int_h^\infty \frac{dh'}{h'^3} \frac{1}{1 - \xi(h')}. \quad (26)$$

Finally, the viscous force on the cantilever is given by the surface integral of the pressure. With $dS = 2\pi dr r = 2\pi R dh$ one finds for the drag coefficient

$$F(h_0) = -2\pi R \int_{h_0}^\infty dh P(h). \quad (27)$$

In eq.(1) we have defined the electroviscous drag coefficient through $F = -\gamma V$; the above relations give

$$\gamma = 12\pi\eta R^2 \int_{h_0}^\infty dh \int_h^\infty \frac{dh'}{h'^3} \frac{1}{1 - \xi(h')}. \quad (28)$$

In the absence of electro-viscous coupling, one readily obtains the pressure

$$P_0(h) = \frac{3\eta V R}{h^2}, \quad (\xi = 0), \quad (29)$$

which is maximum at the centre of the film and vanishes as $P_0 \propto r^{-4}$ at large radial distance. The corresponding lubrication drag coefficient [28],

$$\gamma_0 = \frac{6\pi\eta R^2}{h_0}, \quad (\xi = 0), \quad (30)$$

is by a factor R/h_0 larger than the Stokes drag coefficient $6\pi\eta R V$ on a sphere of radius R in a bulk liquid.

IV. ELECTROVISCOUS DRAG COEFFICIENT

As a main formal result of this paper, eq. (28) expresses the electroviscous drag enhancement in terms of the coupling coefficient ξ which quantifies the charge-flow coupling. Here, we evaluate eq. (28) both analytically and numerically.

A. Wide-channel approximation $h \gg \lambda$

If the height of the water film is much larger than the Debye length, the electrostatic potential is given by [24]

$$\psi = -\frac{4k_B T}{e} \operatorname{arctanh}(\beta e^{-z/\lambda}), \quad (31)$$

where the parameter

$$\beta = \frac{\sqrt{1 + (2\pi\ell_B\lambda\sigma)^2} - 1}{2\pi\ell_B\lambda\sigma} \quad (32)$$

depends on the Debye length λ and the surface charge density σ .

In this case, there are analytical expressions for the transport coefficients L_{ij} . The off-diagonal terms are given by the Helmholtz-Smoluchowski electrophoretic mobility,

$$L_{vc} = -\frac{h\varepsilon\zeta}{e\eta} = -\frac{h\hat{\zeta}}{4\pi\eta\ell_B}, \quad (33)$$

where in the second identity we define the dimensionless zeta potential in units of the thermal energy $\hat{\zeta} = e\zeta/k_B T$. The electrical conductivity reads as

$$L_{cc} = \frac{\sinh(\hat{\zeta}/4)^2}{\pi^2\eta\lambda\ell_B^2} + \sum_{\pm} \mu_{\pm} n_0 \left(h - \frac{4\beta\lambda}{\beta \mp 1} \right), \quad (34)$$

where the first term accounts for electro-osmotic advection and the second for ion electrophoresis, with surface contributions parameterized by β .

For wide channels, $h \gg \lambda$, the conductivity is dominated by bulk ion electrophoresis. Discarding the electro-osmotic and surface terms, and using the definition of the screening length (5), results in the coupling parameter

$$\xi = \frac{\lambda_*^2}{2h^2}, \quad (35)$$

with the length scale

$$\lambda_* = 6\hat{\zeta} \sqrt{\frac{a}{\ell_B}} \lambda. \quad (36)$$

Here and in the following, the mobilities are expressed through ion radii, $\mu_{\pm} = 1/6\pi\eta a_{\pm}$, with the mean value $1/a = 2/a_+ + 2/a_-$.

Then the pressure (26) and the drag coefficient (28) can be integrated in closed form,

$$\frac{\gamma}{\gamma_0} = \frac{h_0}{\lambda_*} \ln \frac{h_0 + \lambda_*}{h_0 - \lambda_*} + \frac{h_0^2}{\lambda_*^2} \ln \frac{h_0^2 - \lambda_*^2}{h_0^2}. \quad (37)$$

In Fig. 2 we plot γ as a (red) solid line. At the distance $h_0 = \lambda_*$ the electroviscous coupling parameter ξ is equal to unity and, as a consequence, a logarithmic branch point appears in the pressure integral (26), resulting in $\gamma/\gamma_0 = 2 \ln 2 \approx 1.39$. At smaller distances the

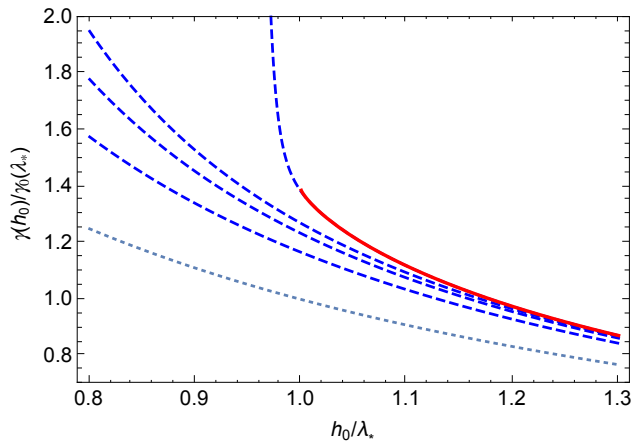


FIG. 2. Electroviscous enhancement of the drag coefficient $\gamma(h_0)$, in units of the purely viscous coefficient γ_0 at $h_0 = \lambda_*$. In the absence of charge-flow coupling as in (30), the dotted line gives $\gamma_0(h_0)/\gamma_0(\lambda_*) = \lambda_*/h_0$. Dashed lines are calculated from the perturbation series (38) for γ , truncated at $(\lambda_*/h_0)^{2n}$ with $n = 1, 2, 3, 100$. The full line represents the complete series (37), which is defined for $h > \lambda_*$ only.

wide-channel approximation for pressure and force integrals is not defined.

It turns out instructive to rewrite (37) as a series in powers of λ_*/h_0 ,

$$\frac{\gamma}{\gamma_0} = 1 + \frac{1}{6} \frac{\lambda_*^2}{h_0^2} + \frac{1}{15} \frac{\lambda_*^4}{h_0^4} + \frac{1}{28} \frac{\lambda_*^6}{h_0^6} + \dots \quad (38)$$

In Fig. 2 we plot this series truncated at $(\lambda_*/h_0)^{2n}$ with $n = 1, 2, 3, 100$, and compare both with (37) and with the uncoupled lubrication drag coefficient (30). Retaining a few terms only, suggests a smooth behavior, whereas Eq. (37) is defined for $h_0 \geq \lambda_*$ only. The first correction term, proportional to λ_*^2/h_0^2 , corresponds to the electroviscous coefficient of Bike and Prieve [15].

Noting that the ion radius is usually smaller than the Bjerrum length $\ell_B = 0.7$ nm, and $\hat{\zeta}$ of the order of unity, one finds that λ_*/λ takes values between 1 and 10.

B. Narrow-channel approximation

In the case of a narrow channel, $h \ll \lambda$, the overlapping double layers of the surfaces result in a constant charge density

$$\rho = \varepsilon \partial_z^2 \psi = 2\sigma/h, \quad (39)$$

in other words, the counterions form a homogeneous gas [24]. The electrostatic potential is readily integrated,

$$\psi(z) = \frac{k_B T}{e} \left(\ln m - \frac{4\pi\ell_B\sigma}{h} z^2 \right), \quad (40)$$

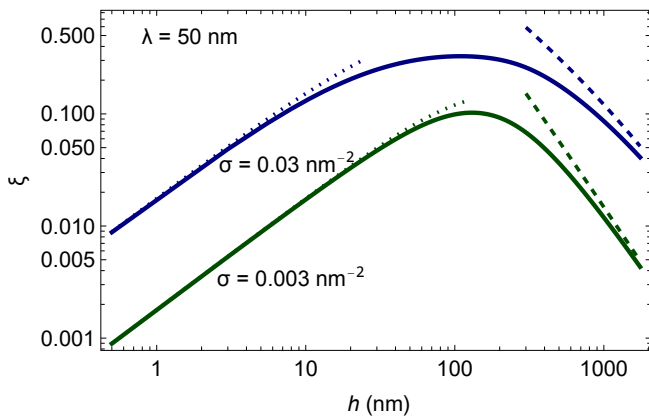


FIG. 3. Numerical calculation of the electroviscous coupling parameter ξ as a function of h , for surface charge density $\sigma = 0.003$ and 0.03 nm^{-2} , and Debye length $\lambda = 50 \text{ nm}$. Dotted and dashed lines correspond to the approximations of narrow and wide channels, respectively, whereas the solid lines give the numerical solution.

where the parameter m describes the finite value of the potential $\psi(0) = (k_B T/e) \ln m$ at $z = 0$.

With these expressions for ρ and ψ the transport coefficients are readily calculated. Retaining contributions of leading order in h only, we find

$$L_{vc} = \frac{e\sigma h^2}{6\eta}, \quad L_{cc} = \frac{e^2\sigma}{3\eta a_+}, \quad (41)$$

resulting in the coupling parameter

$$\xi = \sigma a_+ h. \quad (42)$$

Note that, for narrow channels, the conductivity is independent of salinity and gap height [29], whereas the parameter ξ is linear in h .

C. Numerical evaluation of ξ and γ

In the general case, the electrostatic potential is obtained in terms of the Jacobi elliptic function $\text{cd}(u|m^2)$ [30],

$$\psi(z) = \frac{k_B T}{e} \left[\ln m + 2 \ln \text{cd} \left(\frac{z}{2\lambda\sqrt{m}} \middle| m^2 \right) \right]. \quad (43)$$

Because of $\text{cd}(0|m^2) = 1$, the second term vanishes at $z = 0$, and the potential at $z = 0$ is determined by $\ln m$. The parameter m depends on the ratio of the channel height and the Debye length: For $h \gg \lambda$ one has $m = 1$ and recovers the analytic expression (31) for a charged surface limiting an infinite half-space. In the narrow-channel limit one finds

$$m = \frac{hn_0}{2x\sigma}, \quad (hn_0 \ll \sigma), \quad (44)$$

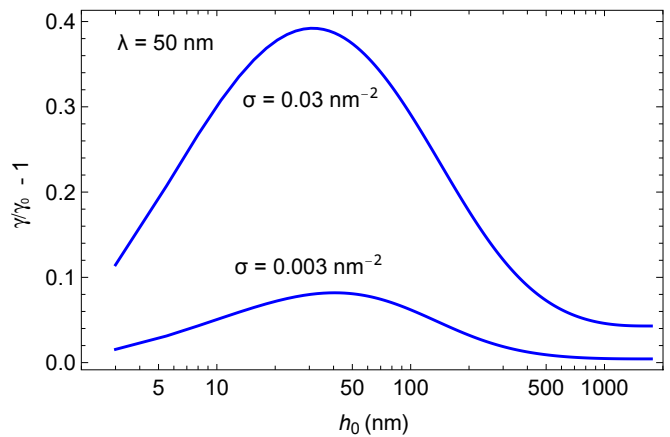


FIG. 4. Electroviscous drag enhancement $\gamma/\gamma_0 - 1$ as a function of h_0 , for different values of the surface charge density σ .

and expanding the Jacobi function to second order in z , one recovers the potential defined in eq. (40) above.

The electric potential is calculated numerically from (43) with the boundary condition (7). Then the electroviscous coupling parameter ξ defined in (25), is obtained by performing the integrals (20) and (21) for a given film distance h . The numerical results are given in terms of the gap height h_0 , the surface charge density σ , and the Debye screening length λ . We use the viscosity of water at room temperature, $\eta = 0.9 \times 10^{-3} \text{ Pa}\cdot\text{s}$, and the ion mobilities $\mu_{\pm} = 1/6\pi\eta a_{\pm}$ with the radii of sodium $a_+ = 1.9 \text{ \AA}$ and of chlorine $a_- = 1.3 \text{ \AA}$ [31].

Fig. 3 shows the variation of ξ as a function of h for different values of surface charge concentration σ , and compares with narrow-channel and wide-channel approximations. As a surprising feature, ξ is roughly linear in σ . The log-log plot shows the power laws $\xi \propto h$ and $\xi \propto h^{-2}$, in the limits of narrow and wide channels, respectively. The maximum occurs at $h_{\text{max}} \approx 3\lambda$. The narrow-channel result (42) provides a good description for $h \leq \lambda$, whereas the wide-channel expression (VII A) converges for $h \gg \lambda_*$ only. In the intermediate range, which covers at least one decade in h , neither of them is valid.

In Fig. 4 we plot the enhancement factor $\gamma/\gamma_0 - 1$ of the viscous force (27), with parameters as in Fig. 3. As expected for the electroviscous coupling parameter ξ , there is a maximum at $h_0 \approx \lambda$. The enhancement factor depends equally strongly on the surface charge and the Debye length.

V. CHARGE REGULATION

So far we have assumed that the surface charge density σ remains constant upon varying the film height h_0 . This is not the case, however, for weakly dissociating acidic groups HA which release and recover protons according

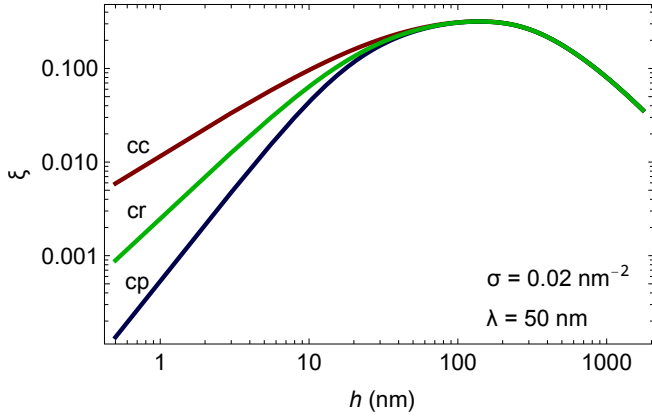
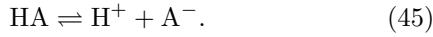


FIG. 5. Electroviscous coupling parameter ξ as a function of the distance h , for constant charge (cc), charge regulation (cr), and constant potential (cp).

to [32]



For narrow channels the potential (43) takes a finite value $\psi(0) = (k_B T/e) \ln m$ at $z = 0$, which favors recombination of the surface groups, thus reducing the effective charge density σ and surface potential ζ .

A simple and widely studied model relies on the dissociation constant

$$\mathcal{Z} = \frac{[\text{H}^+][\text{A}^-]}{[\text{HA}]} = n_s \frac{\alpha}{1 - \alpha}, \quad (46)$$

where we have defined the dissociated fraction α and the hydronium concentration at the surface $n_s = e^{-e\zeta/k_B T} [\text{H}^+]_\infty$. Solving for α one finds the fraction of dissociated sites

$$\alpha = \frac{1}{1 + n_s/\mathcal{Z}}, \quad (47)$$

and the number density of surface charges,

$$\sigma = \frac{\alpha}{S}. \quad (48)$$

The electrostatic potential is obtained by closing the above relations with the boundary condition (7). The area per site S is chosen such that at large distance (where $\zeta = \zeta_\infty$), σ takes the value indicated for the case of constant charge.

An alternate approach, which is often used for systems with more complex charging procedure but essentially leads to the same results, is via a proper minimization of the relevant thermodynamic potential [33].

In the following we compare the electrostatic and electroviscous properties calculated at constant charge (cc) with the charge-regulated case (cr), and also with that of constant potential (cp), where the boundary condition (7) is replaced with

$$\psi(\pm h/2) = \zeta_\infty. \quad (49)$$

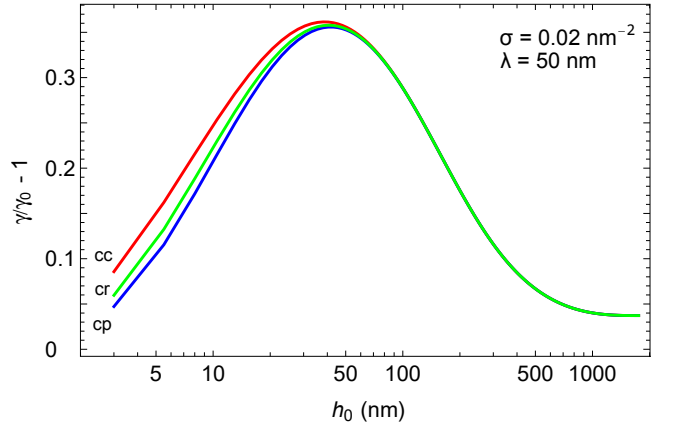


FIG. 6. Electroviscous enhancement $\gamma/\gamma_0 - 1$, as a function of the distance h_0 for different boundary conditions.

Here ζ_∞ is the surface potential at large distance, calculated with the surface charge σ according to (31). All curves labelled “cr” are calculated with $\mathcal{Z} = 10^{-3}$ M.

A. Electroviscous coupling

In Fig. 5 we plot the coupling parameter ξ for the cases of constant charge and constant surface potential, and observe a behavior similar to what has been reported previously for the disjoining pressure [34]: At distances smaller than the screening length, $h < \lambda$, the curves of ξ for different boundary conditions diverge significantly. Yet note that the electroviscous coupling is strongest in the range $\lambda < h < 10\lambda$, where charge regulation is of little importance.

The electroviscous enhancement of the drag force γ with respect to the uncoupled expression γ_0 is shown in Fig. 6. The maximum occurs at a distance slightly below the screening length. For the given electrostatic parameters, it reaches a value of about 35%, which depends little on the electrostatic boundary condition. The electroviscous drag component disappears at much higher distances of about 10λ .

B. Disjoining pressure and static repulsion

Now we consider the static repulsive force arising from the overlap of the diffuse layers on the opposite surfaces, and which is independent of the external driving. According to (43) the potential at $z = 0$ reads as $\psi(0) = (k_B T/e) \ln m$, and the disjoining pressure (8) is determined by the parameter m ,

$$\Pi = n_0 k_B T \left(m + \frac{1}{m} - 2 \right). \quad (50)$$

In Fig. 7 we plot Π calculated for constant charge (cc), constant potential (cp), and charge regulation (cr). For

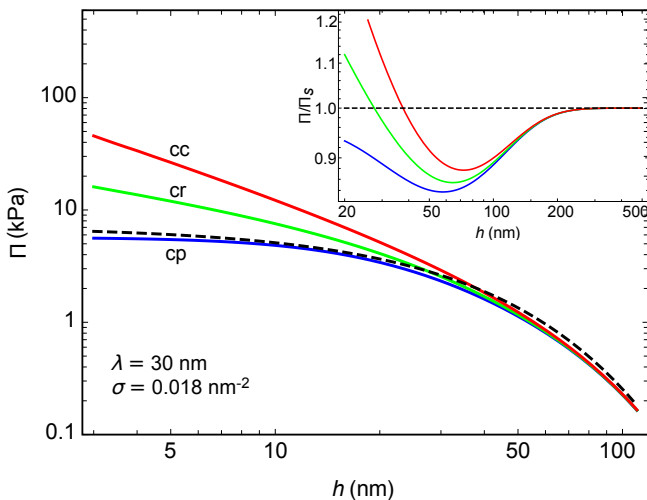


FIG. 7. Disjoining pressure between charged surfaces as a function of the distance h_0 . The solid curves give the numerical solution (8) for constant surface charge $\sigma = 0.018\text{nm}^{-2}$ (cc), constant potential ζ (cp), and the charge-regulated intermediate case (cr) with dissociation constant $\mathcal{Z} = 10^{-3}\text{M}$. The approximative expression (51) is plotted as dashed line. The inset shows the ratio Π/Π_s , highlighting the deviation of the disjoining pressure Π from the approximate expression Π_s , which sets in well above 200 nm.

distances shorter than the screening length, these different boundary conditions result in significant differences. In agreement with previous work, we find a constant pressure for cp [24] and power laws $\Pi \propto h^s$ with $s = -1$ and $-\frac{1}{2}$ for cc and cr, respectively [34].

The dashed line corresponds to the widely used approximation [1]

$$\Pi_s(h) = 64\beta^2 n_0 k_B T e^{-h/\lambda}, \quad (h \gg \lambda), \quad (51)$$

which relies on the linear superposition of the double layers at the opposite surfaces, and where the parameter $\beta = \tanh(e\zeta_\infty/4k_B T)$ is given by the surface potential ζ_∞ at $h_0 \rightarrow \infty$, as defined in eq. (32).

The repulsive force (10) between the two surfaces is calculated in Derjaguin approximation, in analogy to (27), resulting in

$$K = 2\pi R \int_{h_0}^{\infty} dh \Pi(h). \quad (52)$$

For the pressure in superposition approximation we obtain $K_s = 2\pi R \lambda \Pi_s(h_0)$ and, after expressing the salt content through the Debye length,

$$K_s = \frac{16R\beta^2 k_B T}{\lambda \ell_B} e^{-h_0/\lambda}, \quad (h_0 \gg \lambda). \quad (53)$$

A comparison of the numerically exact force K with the exponential approximation K_s is given in Fig. 8. Both expressions agree beyond 200 nm, or $h_0 > 7\lambda$. The

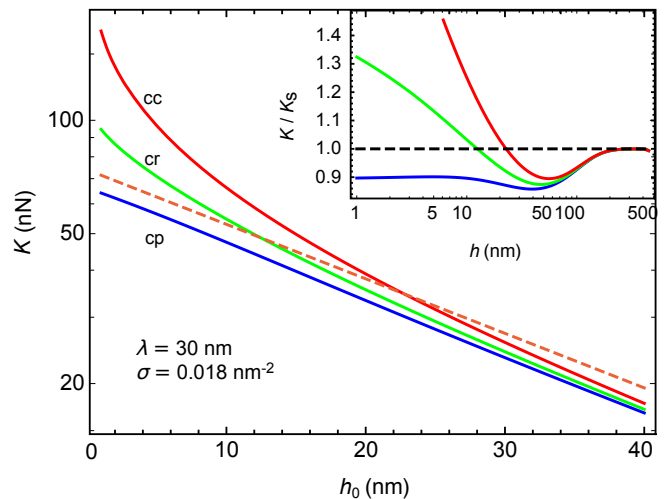


FIG. 8. Static force between charged surfaces as a function of the distance h_0 . The solid curves give the numerical solution (10) for constant charge (upper red), constant potential (lower blue), and charge regulation (middle green). The approximative expression (53) is plotted as dashed line. The inset shows the ratio K/K_s ; note that all curves coincide at large distance, which is not visible in the main figure.

inset shows that the force calculated for constant potential (cp) remains about 10% below K_s , whereas those for constant or regulated charge (cc or cr) show a more complex behavior: they first decrease below K_s yet at even smaller h_0 by far exceed the analytic approximation K_s [1].

VI. AFM FORCE MEASUREMENT

A. Experimental detail

We performed a dynamic AFM measurement with colloidal probe following the method described in [35]. A spherical borosilicate particle (MO-Sci Corporation) with a radius of $R = 47 \pm 1 \mu\text{m}$ was glued at the end of a cantilever (CSG30, NT-MDT) using epoxy (Araldite, Bostik, Coubert). The stiffness of the ensemble of cantilever and particle was calibrated by the drainage method [36], resulting in $k_c = 0.8 \pm 0.1\text{N/m}$. The resonance frequency and bulk quality factor were obtained from the thermal spectrum as $\omega_0/2\pi = 3340\text{ Hz}$ and $Q = 4.7$, respectively.

The experiment was performed using an AFM (Bioscope, Bruker, USA) equipped with a liquid cell (DTFML-DD-HE) which allows us to work in liquid environment. The mica surface was driven by a piezo (Nano T225, MCL Inc., USA) to approach the particle with a very small velocity such that the drainage force can be neglected, and meanwhile the probe was also driven with a base oscillation amplitude $A_b = 3.5\text{ nm}$ and frequency of $\omega/2\pi = 100\text{ Hz}$. The amplitude A and phase φ of the cantilever deflection were measured by a Lock-

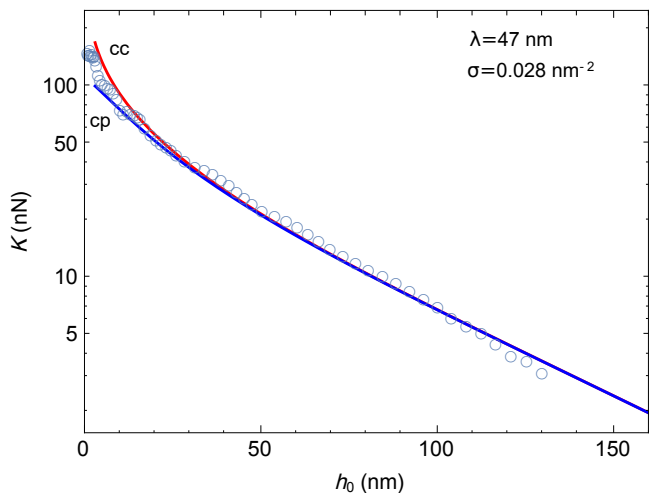


FIG. 9. Static repulsion K between the AFM sphere and the solid surface, as a function of the distance h_0 . The squares give experimental data. The blue and red curves are calculated from (52) for constant potential and constant surface charge, respectively, with the parameter values $R = 55\mu\text{m}$, surface charge density $\sigma = 0.028\text{ nm}^{-2}$ and screening length $\lambda = 47\text{ nm}$.

in Amplifier (Signal recovery, Model:7280), and the DC component of the cantilever deflection was also recorded, from which the separation distance h_0 and electrostatic force K between the sphere and the mica surface were extracted. The mica surface and cantilever probe are immersed in low-salinity water. We also performed control experiments at large salinity. All measurements were done at room temperature 21°C .

B. Static force

Fig. 9 shows the electrostatic repulsive force between the mica surface and the colloidal probe. The data roughly show an exponential behavior, as expected for a screened double-layer interaction. The upper (red) curve is calculated from eq. (52) for constant charge number density $\sigma = 0.028\text{ nm}^{-2}$, and the lower (blue) one for constant surface potential $\zeta = -95\text{ mV}$. In the range where both curves coincide, $h_0 > \lambda$, the best fit is obtained with a screening length $\lambda = 47\text{ nm}$, corresponding to an electrolyte strength $n_0 = 43\mu\text{M}$.

C. Spring constant and drag coefficient

Driving of the probe induces an oscillation of the tip-surface distance according to $h_0 + Z(t)$. Modelling the cantilever as a damped harmonic oscillator [21] and solving its equation of motion for the force F exerted by the

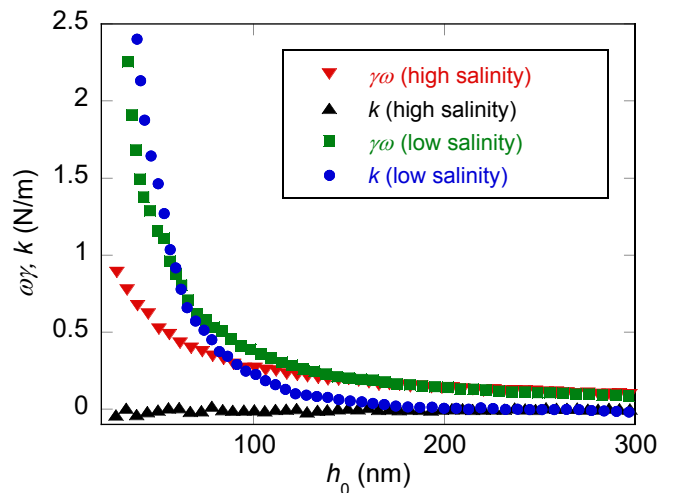


FIG. 10. Real and imaginary parts k and $\omega\gamma$ of the response function, measured at a vibrational frequency $\omega/2\pi = 100\text{ Hz}$ and at low or high salinity, as a function of the distance h_0 .

surrounding liquid, we obtain in complex notation

$$F = -k_c Z \left(1 - \left(\frac{\omega}{\omega_0} \right)^2 + i \frac{\omega}{\omega_0 Q} \right) \frac{A e^{i\varphi} - A_\infty e^{i\varphi_\infty}}{A e^{i\varphi} + A_b}, \quad (54)$$

with amplitude A and phase φ of the mica surface. The tip-surface distance reads as $Z(t) = e^{i\omega t} (A e^{i\varphi} + A_b)$, and the values A_∞ and φ_∞ are measured far from the surface, where the viscoelastic force F is negligible. All measurements are done in the linear-response regime $|Z| \ll h_0$.

In view of eq. (1) we split F/Z in its real and imaginary components. Writing the velocity as $V = i\omega Z$, we readily obtain the complex response function,

$$F = -(k + i\omega\gamma)Z, \quad (55)$$

where the “spring constant” k and the drag coefficient γ account for the elastic and viscous components of the tip-surface interactions.

In Fig. 10 we plot the measured real and imaginary coefficients as a function of the separation distance h_0 at low or high salinity, at the oscillation frequency of $\omega/2\pi = 100\text{ Hz}$. At large salinity electrokinetic effects disappear because of electrostatic screening, and k vanishes accordingly, whereas the drag coefficient follows the law $\gamma_0 \propto 1/h_0$, expected from Stokes hydrodynamics [26]. Quite a different behavior occurs at low salinity, where we observe a strong elastic component k which decays roughly exponentially with h_0 , and an electroviscous enhancement of the drag coefficient.

In Figs. 11 and 12, the experimental findings are compared with theory. Regarding the elastic response, Fig. 11 shows both the static stiffness $-dK/dh_0$ (full symbols) and the dynamic response $k(\omega)$ at finite frequency $\omega/2\pi = 100\text{ Hz}$ (open symbols). The theory curve represents the spring constant (11), which is related to the

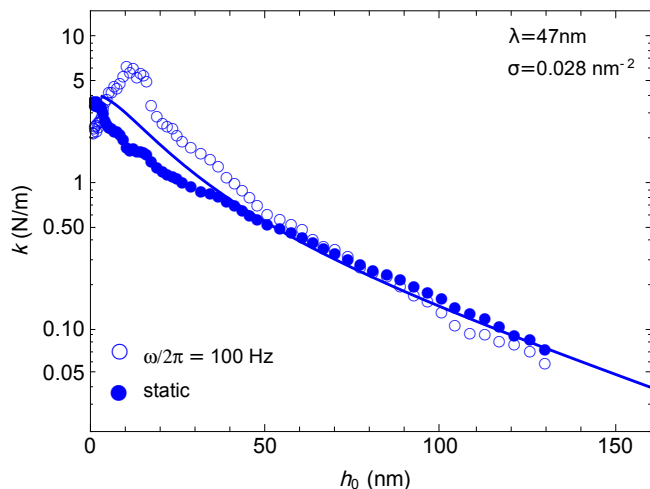


FIG. 11. Elastic response k measured at $\omega/2\pi = 100$ Hz (open symbols) and for the static case (full symbols), as a function of h_0 . The solid line give the static rigidity k , calculated from eq. (11) for constant potential. The experimental data are binned, such that each point corresponds to the mean value of 100 measured values.

variation of the disjoining pressure with distance and which is calculated from (8) at constant potential (cp). The data roughly follow the exponential law expected for double-layer interactions, and they provide strong evidence that the dynamic elastic response $k(\omega)$ comprises a frequency dependent contribution which is most significant at small distances, $h_0 < \lambda$, and which is not captured by the electrostatic disjoining pressure II.

In Fig. 12 we plot the viscous response function $\omega\gamma$. At high salinity, the electric double-layer is thin ($\lambda < 1$ nm), such that charge-flow coupling effects are absent. Indeed, the drag coefficient is well fitted by the viscous contribution $\gamma_0 = 6\pi\eta R^2/h_0$, as expected from (30). At low salinity, the large screening length $\lambda = 47$ nm, comparable to h_0 , results in charge-advection and electroosmotic flow, which increase the hydrodynamic pressure and thus enhance the drag coefficient. The theory curve is calculated numerically from eq. (28), with the same parameters $\sigma = 0.028\text{nm}^2$ and $\lambda = 47$ nm as in Figs. 9 and 11. If the overall behavior of the data is rather well described by the theoretical expression, a significant discrepancy occurs for small gaps, where the data exceed the theoretical curve by up to 60%. Comparison with the elastic coefficient shown in Fig. 11, suggests a frequency dependence of the dynamic response function $k(\omega) + i\omega\gamma(\omega)$, which is not captured by the quasistatic coefficients k and γ derived in the present work.

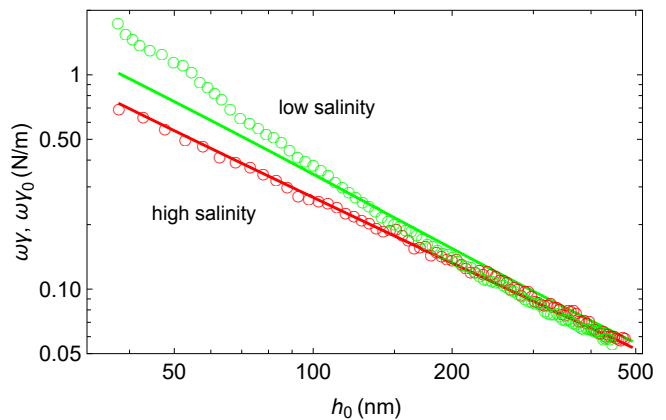


FIG. 12. Comparison of the drag coefficient measured at $\omega/2\pi = 100\text{Hz}$ (circles) with theory (solid curves). At high salinity ($\lambda < 1$ nm, red), the data are well fitted by $\omega\gamma_0$ with the drag coefficient given by (30). At low salinity ($\lambda = 47$ nm, green) we observe a significant electroviscous enhancement, which is qualitatively accounted for by $\omega\gamma$ calculated from (28). For narrow gaps the measured data exceed the theory curve by up to 60%.

VII. DISCUSSION

A. Validity of the wide channel approximation

If the double layers on either side of the water film don't overlap, their properties are given by the Poisson-Boltzmann potential (31) calculated for an infinite half-space. As the surfaces get closer, the diffuse layers start to interact, resulting in electrostatic repulsion and electroviscous coupling. In the range where the distance h_0 is moderately larger than the Debye length λ , widely used approximations result in an exponentially screened electrostatic repulsion [37] and in a power-law dependence of the electroviscous drag [15].

Its range of validity is obviously related to the Debye length λ , yet our analysis shows that in reality it is limited by a significantly larger distance λ_* , defined in (36). With typical values of the ζ -potential ranging from 25 to 100 mV, the parameter λ_* may be up to 10 times larger than the actual screening length λ . This is clearly displayed by the electroviscous coupling parameter plotted in Fig. 3. The wide-channel approximation converges only at $h_0 \gg \lambda$. As a consequence, at distances of the order of or smaller than λ_* , the force can be calculated only numerically.

B. The effect of charge regulation

There are two length scales indicating a qualitative change of the electrostatic properties, as illustrated by the parameter m of the Jacobi elliptic function $\text{cd}(u|m^2)$ in eq. (43), which is plotted in Fig. 13. For very large channels one has $m = 1$, which means that the double

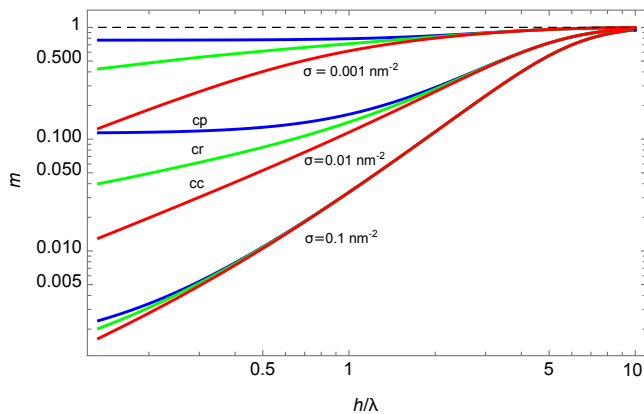


FIG. 13. The parameter m of the electrostatic potential (43) as a function of reduced channel height h/λ , for three values of the surface charge density σ , and for constant charge (cc, red), constant potential (cp, blue), and charge regulation (cr, green). There are two different length scales: The onset of electrostatic coupling of the two diffuse layers, where m starts to decrease below 1, occurs at a distance $h_* = 2\pi\sigma\ell_B\lambda^2$ which increases with σ . On the other hand, the electrostatic boundary condition and charge regulation (cc,cr,cp) are relevant at shorter distances, and there onset occurs at a distance which is inversely proportional to the surface charge density.

layers at opposite surfaces don't interact. The onset of the electrostatic coupling occurs at a film height λ_* which increases with the surface charge density σ , as shown by the curves of Fig. 13.

On the other hand, the electrostatic boundary conditions and charge regulation are relevant at smaller distances, and their onset shows the opposite behavior as a function of the surface charge density. Indeed, for $\sigma = 0.001\text{nm}^{-2}$ the three curves (cc, cp, cr) start diverging at $h = \lambda$, whereas for $\sigma = 0.1\text{nm}^{-2}$ this occurs at much smaller distances.

These features can be observed for both the electrostatic repulsion and electroviscous effects. Regarding the former, the two length scales for the onset of non-exponential behavior and charge regulation effects, are clearly visible in the inset of Fig. 8. Similarly, the electroviscous coupling parameter ξ in Fig. 5 and the enhancement of the drag coefficient in Fig. 6 show characteristic wide-channel power laws for $h \gg \lambda$, whereas charge regulation effects occur at distances shorter than the screening length.

C. Electrokinetic lift force

In this work we have considered the electroviscous force (27) only. As pointed out by Bike and Prieve [15], there is an additional electrokinetic force, given by the diagonal part $\frac{1}{2}\varepsilon E^2$ of the Maxwell stress tensor,

$$F_{\text{el}} = 2\pi R \int_{h_0}^{\infty} dh \frac{\varepsilon E^2}{2}, \quad (56)$$

with the electric field (23). Because of $E \propto V$, this “lift force” is quadratic in the driving velocity $V \propto \cos\omega t$. As a consequence, $F_{\text{el}} \propto \cos^2\omega t$ is always repulsive and oscillates with the double frequency, contrary to the electroviscous force $F = -\gamma V$, which is opposite to the velocity and oscillates with ω .

The present experiments on squeezing motion do not show any indication of the lift force F_{el} . This does not come as a surprise: inserting the wide-channel expressions of the transport coefficients L_{ij} and a typical velocity $V = 100\text{nm/s}$, we find

$$F_{\text{el}} \sim \varepsilon \zeta^2 \left(\frac{\lambda^2 a \eta V R}{h_0^2 k_B T} \right)^2 \sim 10^{-17} \text{N}, \quad (57)$$

which is much smaller than the electroviscous force $F \sim 10^{-9}\text{N}$.

For sliding motion along the surface, on the contrary, the lift force F_{el} turns out to be important. Due to the symmetry properties of the unperturbed pressure P_0 , the corresponding vertical force vanishes, $F = \int dS P_0 = 0$ [15]. Moreover, the horizontal speed \dot{X} of the sliding motion is typically of the order of 10 mm/s, much larger than the vertical velocity $V = \dot{Z}$ in the present experiment.

D. Comparison with previous work

Electroviscous effects on squeezing motion have been studied in several previous papers [15, 21–23]. All of these works start, more or less explicitly, from the volume and charge currents (14) and (15). Yet when calculating the charge current J_C , they use the unperturbed pressure gradient $\nabla P_0 = -6\eta r V/h^3$ instead of ∇P . This perturbative approach corresponds to a linearization of the pressure gradient in the coupling parameter ξ ,

$$\nabla P_1 = \nabla P_0(1 + \xi), \quad (58)$$

instead of the exact expression (24).

As a consequence, electroviscous effects appear as an additive correction to the unperturbed drag force F_0 . Thus the wide-channel force of Bike and Prieve [15] is identical to the first two terms of (38), whereas our expression (37) corresponds to the full series in λ_*/h_0 . Similarly, the numerical calculations of Chun and Ladd [22] and Zhao *et al.* [23], are done with the linearized pressure gradient P_1 .

In Fig. 14 we compare the electroviscous enhancement of the drag force, calculated with the numerically exact pressure gradient (24) and with the linearized form P_1 . For the parameters $\lambda = 50\text{nm}$ and $\sigma = 0.03\text{nm}^{-2}$, the linearized drag coefficient (dashed line) is by 28% larger than γ_0 , whereas the increase of the full expression (solid line) attains 40%. This difference is not surprising in view of the coupling parameters shown in Fig. 3; in the intermediate range where ξ reaches values of the order of unity, one expects a significant nonlinear behavior.

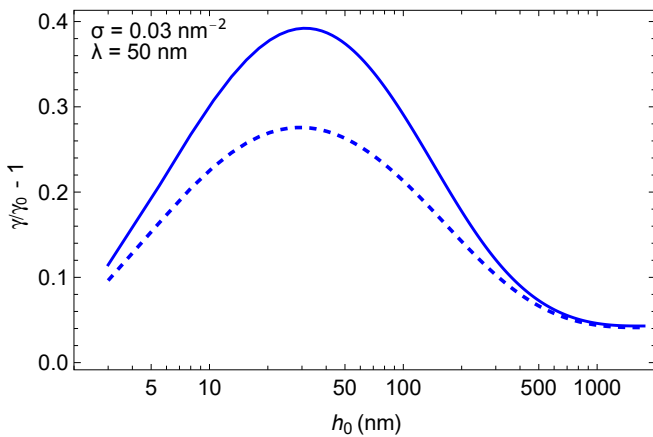


FIG. 14. Numerical calculation of the electroviscous enhancement of the drag coefficient $\gamma/\gamma_0 - 1$ as a function of h_0 , for $\sigma = 0.03\text{nm}^{-2}$ and $\lambda = 50\text{ nm}$. The solid line is calculated with the full pressure (24), and the dashed line that with the linearized expression (58).

VIII. SUMMARY

We have studied the electroviscous and electrostatic forces exerted on a vibrating AFM tip across a nanoscale water film. We briefly summarize the main findings.

(i) In the framework of Onsager relations for generalized fluxes and forces, we derive the drag coefficient (28) in terms of the electroviscous coupling parameter ξ . With the surface charge σ and the screening length λ taken from the electrostatic repulsion (Fig. 9), we find an almost quantitative agreement with experimental data (Fig. 12), with a discrepancy attaining 60% in the narrow-gap limit.

(ii) This analysis relies on a quasistatic approximation (22), where the radial charge distribution in the water film is assumed to follow instantaneously the external

driving. The fits of the viscous and elastic components of the response function (55), measured at $\omega/2\pi = 100\text{ Hz}$ and shown in Figs. 11 and 12, suggest that this approximation is justified at distances larger than the screening length, yet ceases to be valid for $h_0 < \lambda$. Our experimental data strongly suggest that in this range both the spring constant k and the drag coefficient γ vary with frequency. The nature of the underlying relaxation process is not clear at present.

(iii) Previous work relied on the linearization approximation (58) for the hydrodynamic pressure gradient. This linearization significantly underestimates the enhancement of the drag coefficients, for the parameters of Fig. 14 by about 40 %.

(iv) Charge regulation turns out to be of minor importance in the experimentally most relevant range. Indeed, the electroviscous coupling sets in at large distances and is maximum at $h_0 \sim 3\lambda$ (Fig. 3), whereas the electrostatic boundary conditions and charge regulation effects are significant in narrow channels only, as shown in Figs. 5–9.

IX. ACKNOWLEDGEMENTS

This project was supported by the French National Research Agency through Grant No. ANR-19-CE30-0012. MRM acknowledges funding support from the Mexican Council for Science and Technology (CONACYT) Grant No. CVU 625862. ZZ acknowledges funding support from the China Scholarship Council.

*MRM, ZZ and ZB contributed equally to this work.

-
- [1] J. N. Israelachvili, *Intermolecular and surface forces*, 2nd ed. (Academic Press London, San Diego, 1991).
 - [2] J. Israelachvili and H. Wennerström, *Nature* **379**, 219 (1996).
 - [3] J. Lyklema, *Fundamentals of Interface and Colloid Science* (Academic Press, New York, 1995).
 - [4] H. A. Stone, A. D. Stroock, and A. Ajdari, *Annu. Rev. Fluid Mech.* **36**, 381 (2004).
 - [5] J. Yan, M. Han, J. Zhang, C. Xu, E. Luijten, and S. Granick, *Nature materials* **15**, 1095 (2016).
 - [6] S. Marbach and L. Bocquet, *Chem. Soc. Rev.* **48**, 3102 (2019).
 - [7] L. Bocquet and E. Charlaix, *Chemical Reviews* **39**, 1073 (2010).
 - [8] H. Helmholtz, *Annalen der Physik* **243**, 337 (1879).
 - [9] M. von Smoluchowski, *Bull. Akad. Sci. Cracovie.* **8**, 182 (1903).
 - [10] J. J. Bikerman, *Zeitschrift für Elektrochemie und angewandte physikalische Chemie* **39**, 526 (1933).
 - [11] E. Hückel, *Physik. Z.* **25**, 97 (1924).
 - [12] D. C. Henry and A. Lapworth, *Proceedings of the Royal Society of London. Series A* **133**, 106 (1931).
 - [13] R. J. Gross and J. F. Osterle, *The Journal of Chemical Physics* **49**, 228 (1968).
 - [14] B. M. Alexander and D. C. Prieve, *Langmuir* **3**, 788 (1987).
 - [15] S. G. Bike and D. C. Prieve, *Journal of Colloid and Interface Science* **136**, 95 (1990).
 - [16] S. G. Bike and D. C. Prieve, *Journal of Colloid and Interface Science* **154**, 87 (1992).
 - [17] S. G. Bike, L. Lazarro, and D. C. Prieve, *Journal of Colloid and Interface Science* **175**, 411 (1995).
 - [18] S. G. Bike and D. C. Prieve, *Journal of Colloid and Interface Science* **175**, 422 (1995).

- [19] R. Raiteri, M. Grattarola, and H.-J. Butt, *The Journal of Physical Chemistry* **100**, 16700 (1996).
- [20] F. Liu, C. Zhao, F. Mugele, and D. van den Ende, *Nanotechnology* **26**, 385703 (2015).
- [21] F. Liu, A. Klaassen, C. Zhao, F. Mugele, and D. van den Ende, *The Journal of Physical Chemistry B* **122**, 933 (2018), pMID: 28976197.
- [22] B. Chun and A. Ladd, *Journal of Colloid and Interface Science* **274**, 687 (2004).
- [23] C. Zhao, W. Zhang, D. van den Ende, and F. Mugele, *Journal of Fluid Mechanics* **888**, A29 (2020).
- [24] D. Andelman, in *Soft Condensed Matter Physics in Molecular and Cell Biology*, edited by W. Poon and D. Andelman (Taylor & Francis, New York, 2006) pp. 97–122.
- [25] B. Derjaguin, *Kolloid-Zeitschrift* **69**, 155 (1934).
- [26] J. Happel and H. Brenner, *Low Reynolds Number Hydrodynamics* (Martinus Nijhoff, 1963).
- [27] J. L. Anderson, *Annu. Rev. Fluid Mech.* **21**, 61 (1989).
- [28] H. Brenner, *Chem. Eng. Sci.* **16**, 242 (1961).
- [29] D. Stein, M. Kruithof, and C. Dekker, *Physical Review Letters* **93**, 035901 (2004).
- [30] M. Abramowitz and I. A. Stegun, *Handbook of Mathematical Functions* (Dover, New York, 1964).
- [31] L. Bulavin, I. Zhyganiuk, M. Malomuzh, and K. Pankratov, *Ukr. J. Phys.* **56**, 893 (2011).
- [32] B. W. Ninham and V. A. Parsegian, *J. Theor. Biol.* **31**, 405 (1971).
- [33] A. Majee, M. Bier, and R. Podgornik, *Soft Matter* **14**, 985 (2018).
- [34] T. Markovich, D. Andelman, and R. Podgornik, *Europhys. Lett.* **113**, 26004 (2016).
- [35] A. Maali and R. Boisgard, *Journal of Applied Physics* **114**, 144302 (2013).
- [36] V. S. J. Craig and C. Neto, *Langmuir* **17**, 6018 (2001).
- [37] J. Israelachvili, *Journal of Colloid and Interface Science* **110**, 263 (1986).